



On the Construction Methodology of Microabrasion-Corrosion Maps Using Theoretical Approaches

F. W. Ritchie¹ · B. D. Jana² · I. Zekos¹ · M. M. Stack¹

Received: 27 June 2023 / Revised: 6 December 2023 / Accepted: 3 January 2024
© The Author(s) 2024

Abstract

In the field of microabrasion-corrosion, there has been limited research progress in modelling the process due to the complex interplay between the two processes involved. One of the crucial developments in the field has been the microabrasion-corrosion maps based on experimental results. However, mathematical modelling to develop the maps has not been attempted before. This work aimed to construct mathematical models for predicting the microabrasion-corrosion rate for mild steel and pure titanium in aqueous slurry conditions. The methodology developed was used for the construction of microabrasion-corrosion maps. The maps were constructed in two forms: (1) regime maps that identify the underlying mechanisms of microabrasion-corrosion and (2) wastage maps that identify the magnitude of the wastage rate. The effects of abrasive particle size and solution pH were shown on the maps. These maps have not been reported before and can form a basis for material selection and process optimisation for various microabrasion-corrosion applications, such as hip joint conditions. The advantages and applications of these maps are addressed in this paper.

Keywords Microabrasion-corrosion · Modelling · Maps · pH · Particle size

List of Symbols

A	Area undergoing passivation (m^2)	K_{ac}	Combined rate of microabrasion-corrosion ($\text{kg m}^{-2} \text{s}^{-1}$)
b_a	Tafel slope (anode) (V decade^{-1})	K_{ao}	Rate of microabrasion in the absence of corrosion ($\text{kg m}^{-2} \text{s}^{-1}$)
C	Mass concentration of slurry (kg m^{-3})	K_c	Total rate of corrosion ($\text{kg m}^{-2} \text{s}^{-1}$)
E	Applied potential (V)	K_{co}	Rate of corrosion in the absence of microabrasion ($\text{kg m}^{-2} \text{s}^{-1}$)
E_b	Elastic modulus of ball (Pa)	M_t	Mass of target material (kg)
E°	Standard reversible equilibrium potential (V)	n	Number of electrons
E_p	Passivation potential (V)	P	Applied load (N)
E_t	Elastic modulus of target (Pa)	RAM	Relative atomic mass of target (kg)
F	Faraday's constant (C mol^{-1})	R_b	Radius of the ball (m)
H	Thickness of passive film (m)	R_p	Radius of abrasive particles (m)
h^o	Passive film thickness at passivation potential (m)	SCE	Saturated calomel electrode
H_t	Hardness of target (Pa)	ν_b	Poisson's ratio of the ball
i_{anet}	Net anodic current density (A m^{-2})	ν_t	Poisson's ratio of the target
i^o	Exchange current density (A m^{-2})	ΔE	$E - E^\circ$
k_A	Wear coefficient	ΔK_a	Effect of corrosion on the rate of microabrasion ($\text{kg m}^{-2} \text{s}^{-1}$)
K_a	Total rate of microabrasion ($\text{kg m}^{-2} \text{s}^{-1}$)	ΔK_c	Effect of microabrasion on the rate of corrosion ($\text{kg m}^{-2} \text{s}^{-1}$)
		ρ_f	Density of passive film (kg m^{-3})
		ρ_p	Density of abrasive particles (kg m^{-3})
		ρ_t	Density of target material (kg m^{-3})
		ω	Angular velocity of the ball (rad s^{-1})

✉ B. D. Jana
b.jana@shu.ac.uk

¹ Department of Mechanical & Aerospace Engineering, James Weir Building, 75 Montrose Street, Glasgow G1 1XJ, UK

² Department of Engineering and Mathematics, Sheffield Hallam University, City Campus, Howard Street, Sheffield S1 1WB, UK

1 Introduction

Microabrasion-corrosion causes material surface degradation in various applications, ranging from offshore to healthcare. For example, microabrasion-corrosion can lead to premature failure of artificial joints such as hip or knee prostheses. When the process occurs on these implants, there can be an accumulation of abrasive particles up to 10 μm in size on the surface of the implant. This can lead to wear taking place at relatively low loads through the process of microabrasion-corrosion [1].

In the literature, extensive laboratory-based experimental studies have been reported on both microabrasion and microabrasion-corrosion behaviour of different materials under varied tribological conditions [1–3]. Most of these experimental studies have used a micro-scale abrasion test (also known as the ball-cratering abrasive wear test), in which a ball rotates against a specimen, and a slurry of fine abrasive particles is fed at the ball-specimen contact. The theories and models developed in the field of microabrasion have been mainly based on the above experimental setup, and the modelling work attempted here was also based on this setup. As wear is heavily dependent on system properties, and caution must be taken when considering a microabrasion-corrosion application that is different from the ball-cratering test.

The interaction between the two processes of microabrasion and corrosion is now well understood. There are two possible interactions: (1) the "synergistic" effect of corrosion on the microabrasion and (2) the "additive" effect of microabrasion on the corrosion [2]. The synergistic effect refers to corrosion reducing microabrasion resistance by the formation of a fragile corrosion/passivation film on the target surface. However, when the corrosion product is stable and durable, microabrasion resistance can be enhanced. In that case, the value of the synergistic component is negative, and the mechanism is then referred to as the "antagonistic" effect [4]. The additive effect can appear through a mechanism when the microabrasion process enhances the corrosion rate. That can happen when abrasive particles remove any inherent protective oxide film from the target surface, causing an increase in the corrosion rate.

Significant research progress has been made in the field of microabrasion alone [1, 5, 6]. The mechanisms of microabrasion can be two-body or three-body abrasion [2]. During two-body abrasion, the abrasive particles adhere to one surface, creating deep linear grooves on the other surface [2]. Two-body abrasion can usually be seen at high applied load levels for low concentrations of abrasive

particles [5]. During the process of three-body abrasion, the abrasive particles roll between the two sliding surfaces, creating multiple indentations on both surfaces without a clear pattern or direction [2]. Three-body abrasion can usually be seen at low applied load levels for high concentrations of abrasive particles [5]. In this study, material microabrasion loss was considered due to the three-body abrasion mechanism and, therefore, is synonymous with three-body abrasion.

In relation to mathematical modelling in the fields of both microabrasion and microabrasion-corrosion, there has been limited progress. In the field of microabrasion-corrosion, there have been virtually no mathematical modelling studies except a published report on the use of neural networks to predict lab results [7]. However, using neural networks remains challenging as insufficient experimental data are currently available to train the software [7]. On the contrary, modelling of the microabrasion process (without the effect of corrosion) has been studied extensively; however, the modelling approach primarily relied on the use of Archard equations with an effort particularly to modify the wear coefficient for metallic and non-metallic coating systems [8–12].

Although there is demand for the development of predictive mathematical models for the microabrasion-corrosion process, fulling that is difficult mainly because of the complex interplay between the microabrasion and the corrosion process involved. One of the ways to simplify the complexity could be by considering the modelling approach based on tribo-corrosion mapping already established for other tribological processes, such as erosion-corrosion [13]. Theoretical microabrasion-corrosion maps have not been reported before and are of high importance in predicting the regimes and rates of wastage that can lead to the formulation of a degradation mitigation method or appropriate material selection strategy.

The objective of this paper was to construct predictive mathematical models for microabrasion-corrosion and finally use those for the construction of theoretical microabrasion-corrosion maps. Maps were presented in two different forms: (1) "regime" maps that identify different mechanisms of microabrasion-corrosion and (2) "wastage" maps that predict the rate of degradation as high, medium, and low. Maps were constructed for mild steel and pure titanium, referred to as Fe and Ti. Tribo-corrosion responses of these two materials were compared at several different microabrasion-corrosion conditions.

2 Methodology

2.1 Model Creation

2.1.1 List of Assumptions

In this modelling study, the following simplistic assumptions were made.

- (i) The microabrasion process was considered as the test configuration used in a ball-catering wear tester [2]; majority of the models used in this work are based on this test configuration.
- (ii) Target materials were mild steel and pure titanium, and ball material was polypropylene. [Although consideration of actual biomaterial grades, such as stainless steel and Ti-alloy, could have been most appropriate, published data for the extensively different mechanical and corrosion property values (Tables 1, 2, 3) required for this mathematical modelling study were not available for these materials].
- (iii) The abrasive particles used were silicon carbide particles and they were assumed spherical.
- (iv) The concentration of the abrasive particles in the aqueous solution was 25 kg m^{-3} .
- (v) During the microabrasion process, the concentration of slurry (supplied from an external source) remained the same at the contact area between the ball and the specimen. Although in some cases clumping of abrasive particles, giving rise to a variation in slurry concentrations at the contact area, is possible; however, this effect was neglected in this study.
- (vi) At the ball-specimen contact, there was a continuous flow of slurry
- (vii) The concentration of abrasive particles in the aqueous solution always remained constant.
- (viii) The abrasive particles had hardness greater than that of the ball and the target.
- (ix) The metal ion concentration in equilibrium with the target material was 10^{-6} molar.
- (x) The aqueous solution used was water.
- (xi) In the active corrosion conditions, there was no corrosion products or passive films on the target surface.
- (xii) The passivation process was instantaneous through the formation an oxide film on the target surface;

Ti passivated through the formation of TiO_2 , and Fe passivated through the formation of Fe_2O_3 .

- (xiii) In the passivation conditions, there was no subsequent dissolution of the passive film.
- (xiv) The microabrasion-corrosion process was additive in the passive conditions when the microabrasion process enhanced the corrosion rate due to the removal and reformation of the passive film.

2.1.2 Criteria for Defining the Microabrasion-Corrosion Regimes

The total rate of metal wastage under microabrasion-corrosion conditions (K_{ac}) can be expressed as [1, 6, 14].

$$K_{ac} = K_a + K_c \quad (1)$$

where K_a is the total microabrasion rate and K_c is the total corrosion rate.

As there is an interaction between the microabrasion and corrosion process, the total rate of corrosion and microabrasion (in Eq. 1) can be given as

$$K_a = K_{a0} + \Delta K_a \quad (2)$$

$$K_c = K_{c0} + \Delta K_c, \quad (3)$$

where K_{a0} is the rate of microabrasion in the absence of corrosion, ΔK_a is the change in the rate of microabrasion due to the influence of corrosion (i.e. the synergistic effect) [4], K_{c0} is the rate of corrosion in the absence of microabrasion and ΔK_c is the change in the rate of corrosion due to the influence of microabrasion (i.e. the additive effect) [4].

By substituting Eqs. 2 and 3 into Eq. 1, a complete expression for the total microabrasion-corrosion rate can be obtained as follows:

$$K_{ac} = K_{a0} + \Delta K_a + K_{c0} + \Delta K_c \quad (4)$$

For the active region of metal dissolution, it was assumed that both the synergistic and additive effects of the microabrasion and corrosion interaction are not significant and, therefore, can be negligible. However, for the passive region, the additive effect of microabrasion on corrosion is significant as the passive film is likely to provide some resistance to the metal dissolution process, especially under mild abrasive conditions when passive film removal and reformation are possible. However, the synergistic effect of corrosion on microabrasion is very complex and assumed in this study to be negligible in the passive region. Therefore, for the active region,

$$K_a = K_{a0} \quad (5)$$

Table 1 Hardness values of materials modelled

Material	Hardness (Pa)	References
Iron	8.2×10^8	[13]
Titanium	2.25×10^9	[19]

$$K_c = K_{co} \quad (6)$$

and for the passive region,

$$K_a = K_{ao} \quad (7)$$

$$K_c = \Delta K_c \quad (8)$$

2.1.3 Determination of the Rate of Microabrasion ($K_c = K_{ao}$) in the Units of $\text{kg m}^{-2} \text{s}^{-1}$

For the work in this paper, microabrasion rate was calculated using the model developed by Rabinowicz et al. [15]. The model is based on a simple theory of three-body abrasive wear for a rounded abrasive particle creating a groove in the target over a given sliding distance. The final expression developed by Rabinowicz et al. for the volume loss (V) per unit sliding distance (L) is given below:

$$\frac{dV}{dL} = \frac{k_A P}{3H_t}, \quad (9)$$

where k_A is the wear coefficient, P is the applied load and H_t is the hardness of the target.

Please note, Eq. 9 is similar in form to Archard's equation [8].

Equation 9 was then modified to calculate the mass of target material lost (m) per unit time (t) as follows:

$$\frac{dm}{dt} = \frac{k_A P \rho_t R_b \omega}{3H_t}, \quad (10)$$

where ρ_t is the density of the target, R_b is the radius of the ball and ω is the balls angular velocity.

During the micro-abrasion process, the wear loss is contributed by the number of abrasive particles per area of contact (N1). This can be expressed from the particle concentration at the contact.

$$N_1 = \frac{(\text{mass concentration of slurry}) * (\text{diameter of abrasive particle})}{(\text{mass of abrasive particle})}$$

$$N_1 = \frac{C}{\frac{2}{3}\pi R_p^2 \rho_p}, \quad (11)$$

where C is the concentration of slurry, R_p is the radius of abrasive particles and ρ_p is the density of abrasive particles.

It was then possible to find the rate of microabrasion, K_a (or K_{ao}), in the absence of corrosion in units of $\text{kg m}^{-2} \text{s}^{-1}$ by multiplying Eq. 10 (expressed in kg s^{-1}) to Eq. 11 (expressed in m^{-2}), and the final expression can be given as

$$K_a = K_{ao} = \frac{1}{2\pi} \frac{k_A P \rho_t R_b \omega C}{H_t R_p^2 \rho_p} \quad (12)$$

Further to the assumptions listed in 2.1.1, in deriving Eq. 12, it was assumed that the separation distance between the ball and the specimen is equal to or less than the diameter of the abrasive particles.

2.1.4 Determination of the Rate of Corrosion ($K_c = K_{co}$) in the Active Corrosion Media (in the Units of $\text{kg m}^{-2} \text{s}^{-1}$)

The rate of corrosion in the absence of the effects of microabrasion, K_c (or K_{co}), can be given as [13]:

$$K_c = K_{co} = \frac{RAM(i_{anet})}{nF}, \quad (13)$$

where

$$i_{anet} = i_o \left(\exp \left[\frac{2.303(\Delta E)}{b_a} \right] - \exp \left[\frac{2.303(-\Delta E)}{b_c} \right] \right), \quad (14)$$

where RAM is the relative atomic mass of target material, i_{anet} is the net anodic current density for the metal dissolution under activation-controlled conditions, F is the Faradays constant, i_o is the exchange current density, b_a and b_c are the Tafel slope value for both the anode and cathode, respectively and ΔE is the difference between the applied potential and the standard reversible equilibrium potential.

Equation 13 is expressed in $\text{kg m}^{-2} \text{s}^{-1}$. In this work, the number of electrons, n, for both the iron and titanium metals considered in this study was considered as 2.

2.1.5 Determination of the Rate of Corrosion ($K_c = \Delta K_c$) in the Passive Corrosion Media (in the Units of $\text{kg m}^{-2} \text{s}^{-1}$)

It can be seen from Eqs. 5–8 that the corrosion in the passive region was assumed to be entirely contributed by the additive effect of microabrasion on the corrosion rate (ΔK_c). In the passive conditions, the process of passivation and microabrasion acts simultaneously; ΔK_c was, therefore, assumed to be the rate of re-passivation over the abraded surface formed due to microabrasion.

To model this behaviour, the area of re-passivation needs to be determined. In a ball-cratering abrasive wear test, according to Adachi and Hutchings [2], in three-body abrasion conditions, the initial contact area between the ball and target specimen (for one ball rotation) can be given as

$$A = \pi [a^2 + 4R_b R_p], \quad (15)$$

where R_b is the radius of the ball and R_p is the radius of the abrasive particles, and a is the radius of the Hertzian contact area [16], which can be given as

$$a = \left(\frac{3PR_b}{4E^*} \right)^{1/3}, \tag{16}$$

where

$$\frac{1}{E^*} = \frac{(1 - \nu_t^2)}{E_t} + \frac{(1 - \nu_b^2)}{E_b} \tag{17}$$

and E_t and E_b are the Young's moduli and ν_t and ν_b are the Poisson's ratios of the target and the ball, respectively.

The contact area (in Eq. 15) is the area of the target material that is subjected to re-passivation process during a ball-cratering abrasive wear test [2]. Hence, the mass of passive oxide film (M_f) produced on the target surface can be given as

$$M_f = \pi \left[\left(\frac{3PR_b}{4E^*} \right)^{2/3} + 4R_bR_p \right] h\rho_f, \tag{18}$$

where ρ_f is the density of passive film and h is the passive film thickness, which can be given as [13]:

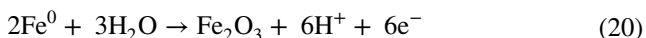
$$h = h^o + 3 * 10^{-9} (E - E_p), \tag{19}$$

where $h^o = 10^{-9}m$ and E_p is the passivation potential.

The passive film was assumed to form instantly on the surface of the target material when the applied potential is equal to the passivation potential [13, 17]. The passive film thickness was assumed to increase by 3nm per volt of overpotential [13, 17].

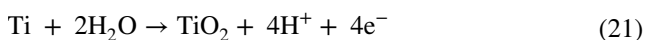
The mass of target material required to form the passive film can be calculated based on the mass ratio between the target material and the passive film.

For iron (Fe) at the modelled conditions of pH 3, 7 and 9, passivation was assumed to take place according to the following reaction,



and the mass ratio between Fe^0 and Fe_2O_3 is equal to 0.699.

For Titanium (Ti), at the modelled conditions of pH 3, 7 and 9, the passivation reaction was assumed as



and the mass ratio between Ti^0 and TiO_2 is equal to 0.5997.

Therefore, the mass target required (M_t) to passivate per rotation of the ball can be given as

$$M_t = \text{Mass Ratio} * \pi \left[\left(\frac{3PR_b}{4E^*} \right)^{2/3} + 4R_bR_p \right] h\rho_f \tag{22}$$

The rate of corrosion in the passive region K_c (or ΔK_c) can be expressed in the unit of $kg\ m^{-2}\ s^{-1}$ by multiplying Eq. 22 by the number of abrasive particle (N_2) present at the ball-specimen contact per $m^{-2}\ s^{-1}$.

$$N_2 = \frac{\text{Particle flux at the contact due angular velocity of the ball}}{\text{Mass of abrasive particle}}$$

$$N_2 = \frac{CR_b\omega}{\frac{4}{3}\pi R_p^3\rho_p} \tag{23}$$

Finally, an expression for the rate of corrosion in the passive region K_c (or ΔK_c) can be derived by multiplying Eq. 22 with Eq. 23, and can be given as

$$K_c = \Delta K_c = \frac{\text{Mass Ratio} \pi \left[\left(\frac{3PR_b}{4E^*} \right)^{2/3} + 4R_bR_p \right] h\rho_f CR_b\omega}{\frac{4}{3}\pi R_p^3\rho_p} \tag{24}$$

2.1.6 Determination of Passivation Potentials for Pure Fe and Ti at Various pH and Potential Range

To find the passivation potential of Fe and Ti, simplified Pourbaix diagrams of the metals were used (Figs. 1, 2) [18]. The passivation potential is a potential at which thermodynamically stable passive oxide layer forms on the target

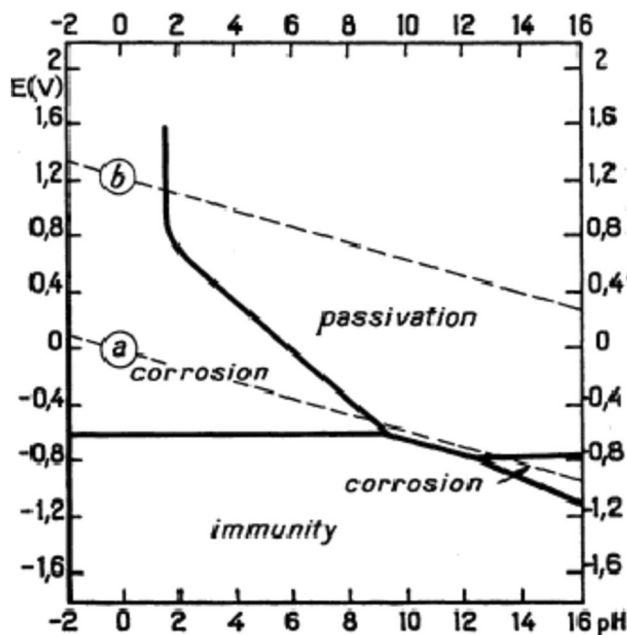
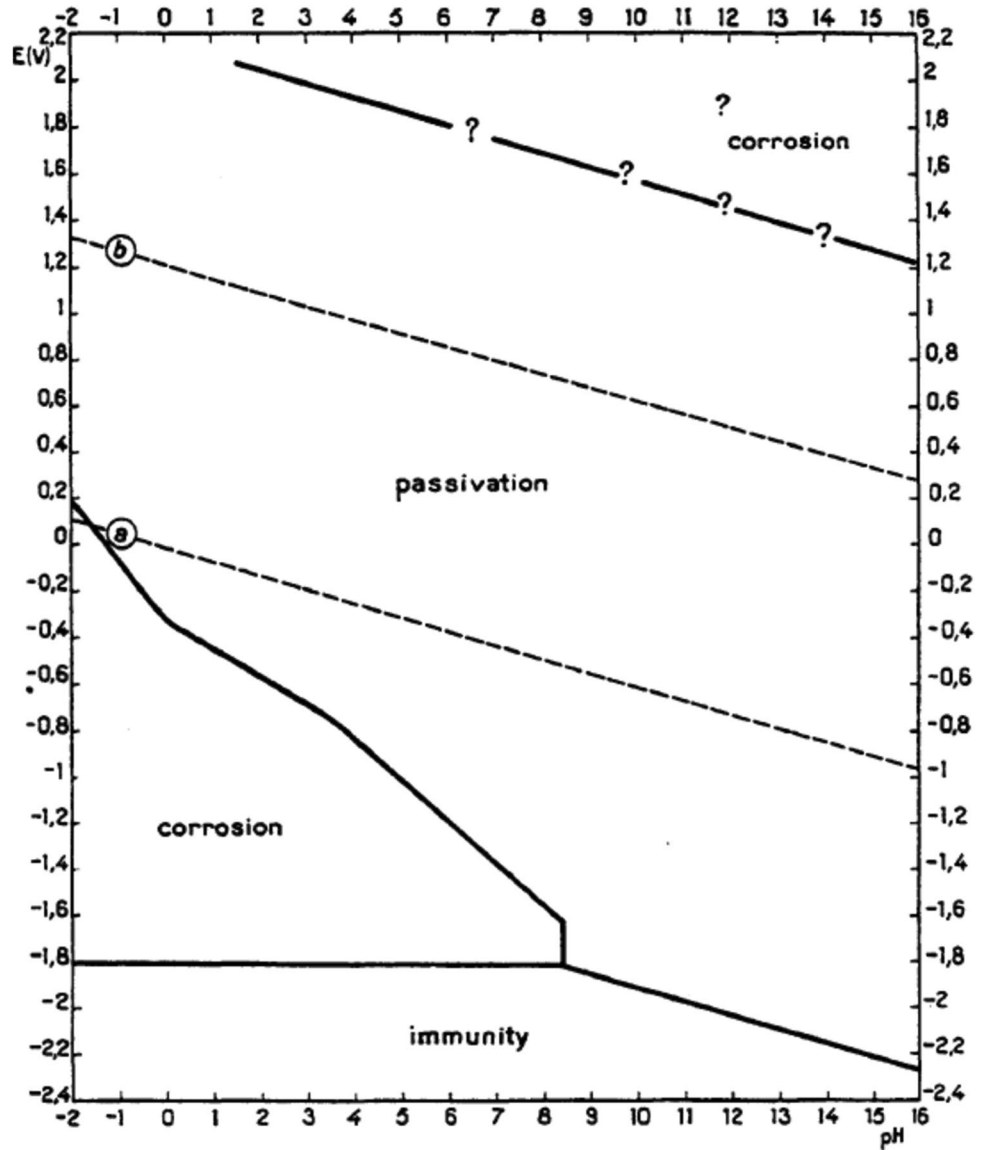


Fig. 1 Pourbaix diagram for Fe [18]

Fig. 2 Pourbaix diagram for Ti [18]



surface. Based on the simplified Pourbaix diagram of Fe and Ti in water, in Figs. 1 and 2 [18], the passivation potential for Fe is the potential at which Fe₂O₃ formation is thermodynamically stable. Thus, the passivation potential (E_p) for Fe can be given as

$$E_p = 1.08 - 0.177pH \tag{25}$$

Equation 25 is expressed in SHE volts, and is valid for the pH 3, 7 and 9 considered in this modelling study.

Whereas, for Ti the passivation potential is the potential at which TiO₂ formation is thermodynamically stable. Hence, the passivation potential (E_p) for Ti at the modelled condition of pH 3 and 7 can be given as

$$E_p = -0.325 - 0.1182pH \tag{26}$$

whereas the passivation potential (E_p) for Ti at the modelled condition of pH 9 can be given as

$$E_p = -1.306 - 0.0591pH \tag{27}$$

2.1.7 Boundary Conditions for the Regime and Wastage Maps

For the construction of regime maps, the following boundary conditions [1] were used particularly for the determination of the regime boundaries as a function of applied load and applied potential.

$$\left(\frac{K_c}{K_a}\right) < 0.1 \text{ (Microabrasion)}$$

Table 2 Density of passive films formed

Material	Passive film forming	Density of film (Kg m ⁻³)	References
Iron	Fe ₂ O ₃	5240	[13]
Titanium	TiO ₂	4230	[20]

Table 3 Constants used to construct regime and wastage maps

Variable	Values			
	Fe	References	Ti	References
<i>i</i> ^o	10 ⁻⁴	[13]	7 × 10 ⁻⁴	[21]
<i>b</i> _a	0.04	[13]	0.06	[22]
<i>ρ</i> _p	3210	[13]	3210	[13]
<i>ρ</i> _t	7800	[13]	4506	[23]
<i>R</i> _p	0.0125	[1]	0.0125	[1]
<i>R</i> _b	10 ⁻⁴	[1]	10 ⁻⁴	[1]
<i>ω</i>	10.472		10.472	
<i>E</i> _t	2.11 × 10 ¹¹	[13]	1.03 × 10 ¹¹	[24]
<i>v</i> _t	0.293	[13]	0.34	[25]
<i>E</i> _b	1.50 × 10 ⁹	[2]	1.50 × 10 ⁹	[2]
<i>v</i> _b	0.4	[2]	0.4	[2]
<i>k</i> _a	2 × 10 ⁻³	[15]	2 × 10 ⁻³	[15]

$$0.1 \leq \left(\frac{K_c}{K_a}\right) < 1 \text{ (Microabrasion–Corrosion)}$$

$$1 \leq \left(\frac{K_c}{K_a}\right) < 10 \text{ (Corrosion–Microabrasion)}$$

$$\left(\frac{K_c}{K_a}\right) > 10 \text{ (Corrosion)}$$

For the wastage maps, the following boundary conditions [13] were used particularly for the determination of the Low, Medium and High wastage contours.

$$K_{ac} < 1 \text{ mm per year (Low wastage)}$$

$$1 \leq K_{ac} < 10 \text{ mm per year (Medium wastage)}$$

$$K_{ac} > 10 \text{ mm per year (High wastage)}$$

As per the boundary conditions, the expressions for *K*_a and *K*_c (i.e. Equation 12, 13 and 24) were combined and rearranged to find an expression for the transition load. The calculation for the transition load is shown below.

2.1.8 Calculation of Transition Load for the Regime and Wastage Maps

For the active region, the expression for the transition load (*P*) is given in Eq. 28. The transition load was calculated for every value of *i*_{anet} for each of the three boundary conditions set for the regime map:

$$P = \frac{2\pi H_t R_p^2 \rho_p RAM i_{anet}}{k_A \rho_t R_b \omega C \left(\frac{K_c}{K_a}\right) nF} \tag{28}$$

For the passive region, the expression for the transition load (*P*) is given in Eq. 29. The transition load was calculated for every thickness of passive film for each of the boundary conditions for the regime map:

$$\frac{K_c}{K_a} = \frac{3 \text{Mass Ratio } \pi H_t h \rho_f \left[\left(\frac{3PR_b}{4E^*}\right)^{2/3} + 4R_b R_p \right]}{2R_p k_a P \rho_t} \tag{29}$$

To calculate the transition load (*P*) in Eq. 29, MATLAB 2020a was used to perform the iteration. Microsoft Excel was used to do the necessary calculations and construction of the regime maps.

To find the transition loads for the wastage maps, the process differed slightly.

For active region, the expression for the transition load is given in Eq. 30.

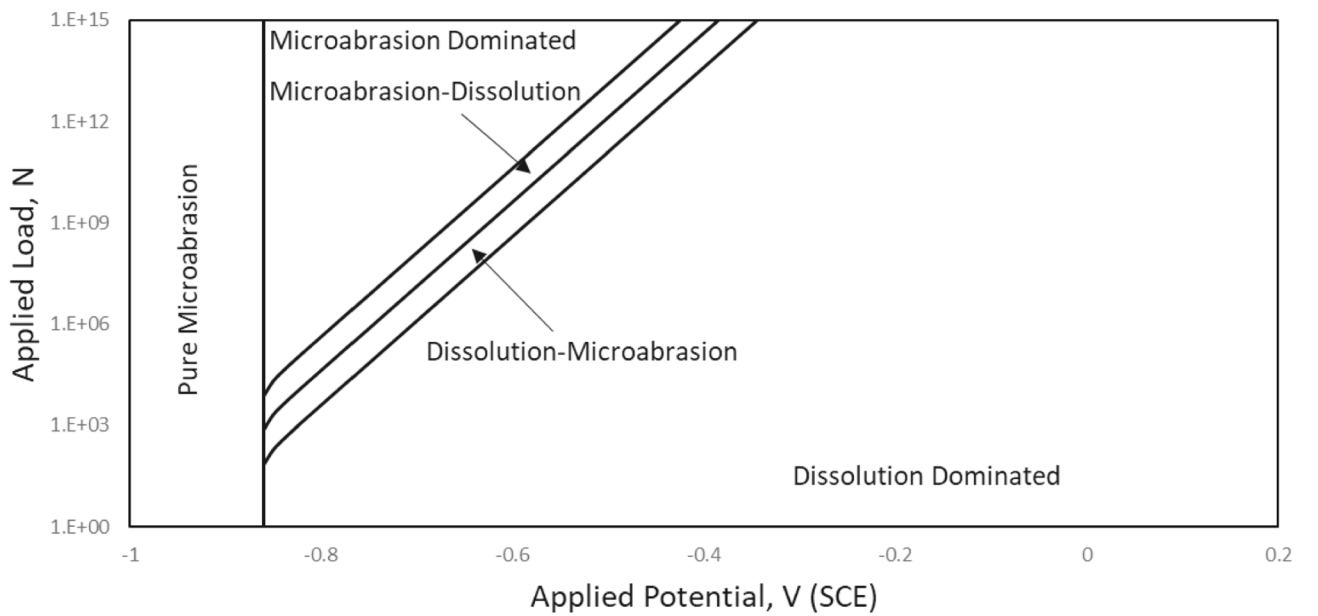
$$K_{ac} = K_c + K_a = \frac{RAM(i_{anet})}{nF} + \left(\frac{1}{2\pi}\right) \frac{K_a P \rho_t R_b \omega C}{H_t R_p^2 \rho_p} \tag{30}$$

For the passive region, the expression for the transition load is given in Eq. 31.

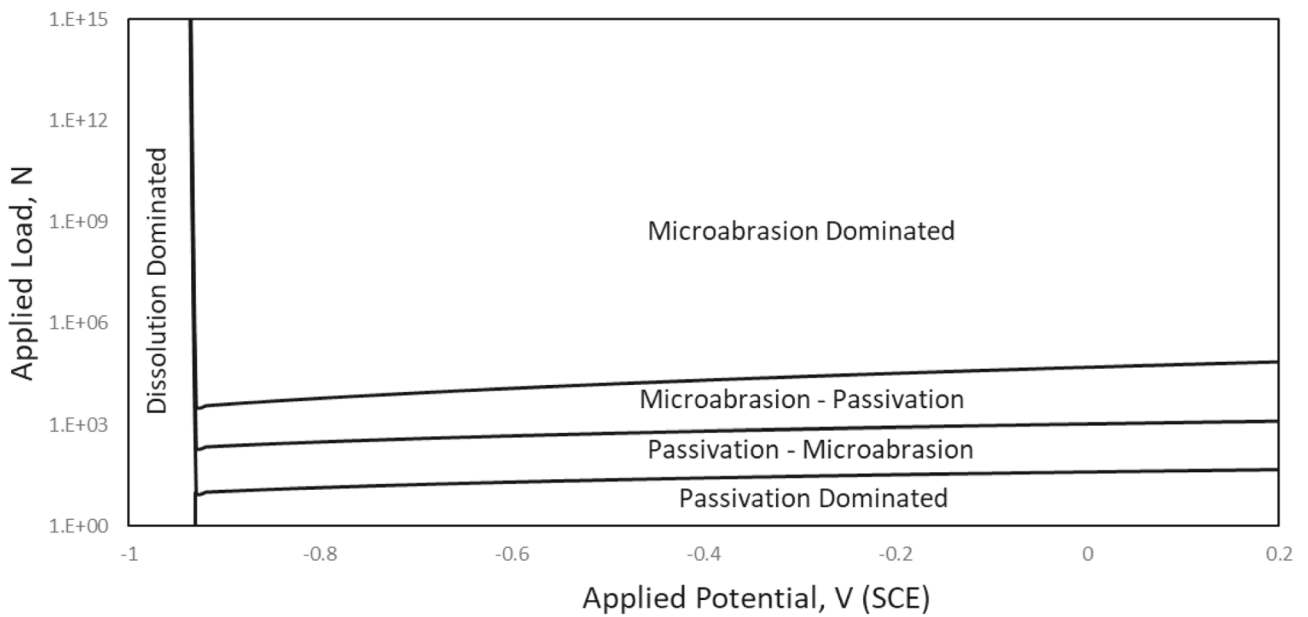
$$K_{ac} = \Delta K_c + K_a = \frac{\text{Mass Ratio } \pi \left[\left(\frac{3PR_b}{4E^*}\right)^{2/3} + 4R_b R_p \right] h \rho_f C R_b \omega}{\frac{4}{3} \pi R_p^3 \rho_p} + \left(\frac{1}{2\pi}\right) \frac{k_a P \rho_t R_b \omega C}{H_t R_p^2 \rho_p} \tag{31}$$

Finally, Microsoft Excel was used to do the necessary calculations and construction of the regime and wastage maps in the form of applied load vs applied potential plots.

The other conditions used for the construction of maps are shown in Table 1, 2 and 3.



(a)



(b)

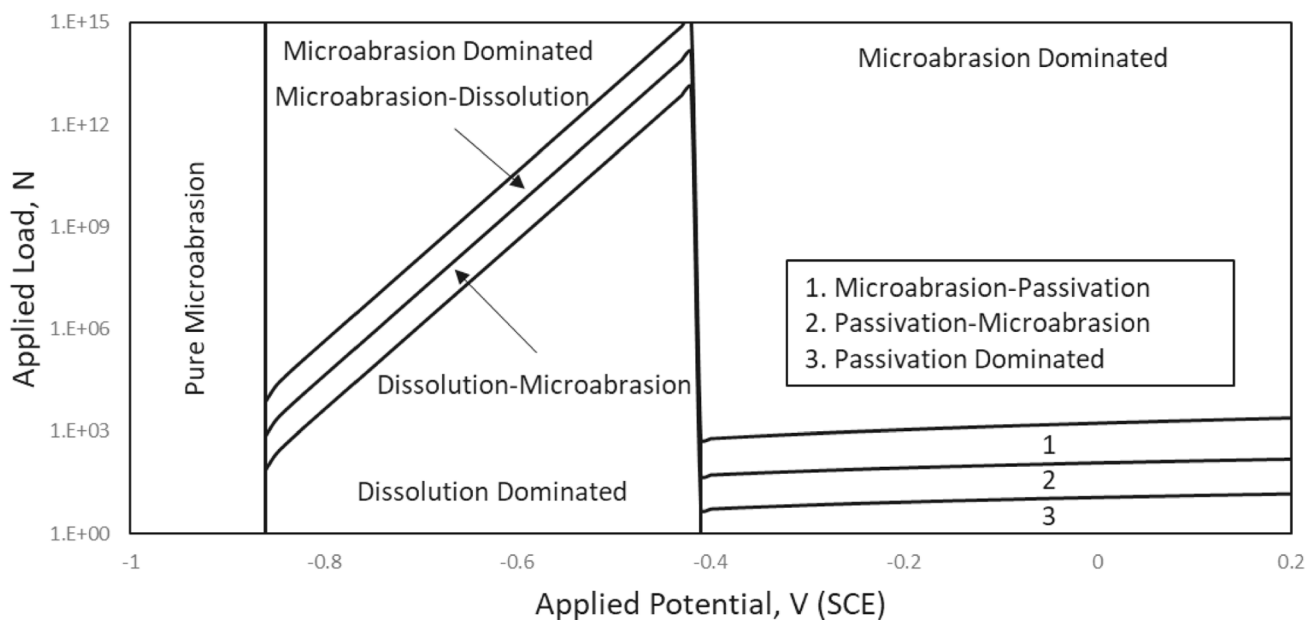
Fig. 3 Applied load—applied potential regime maps for **a** Fe and **b** Ti under solution pH 3 and particle size of 100 μm

3 Results

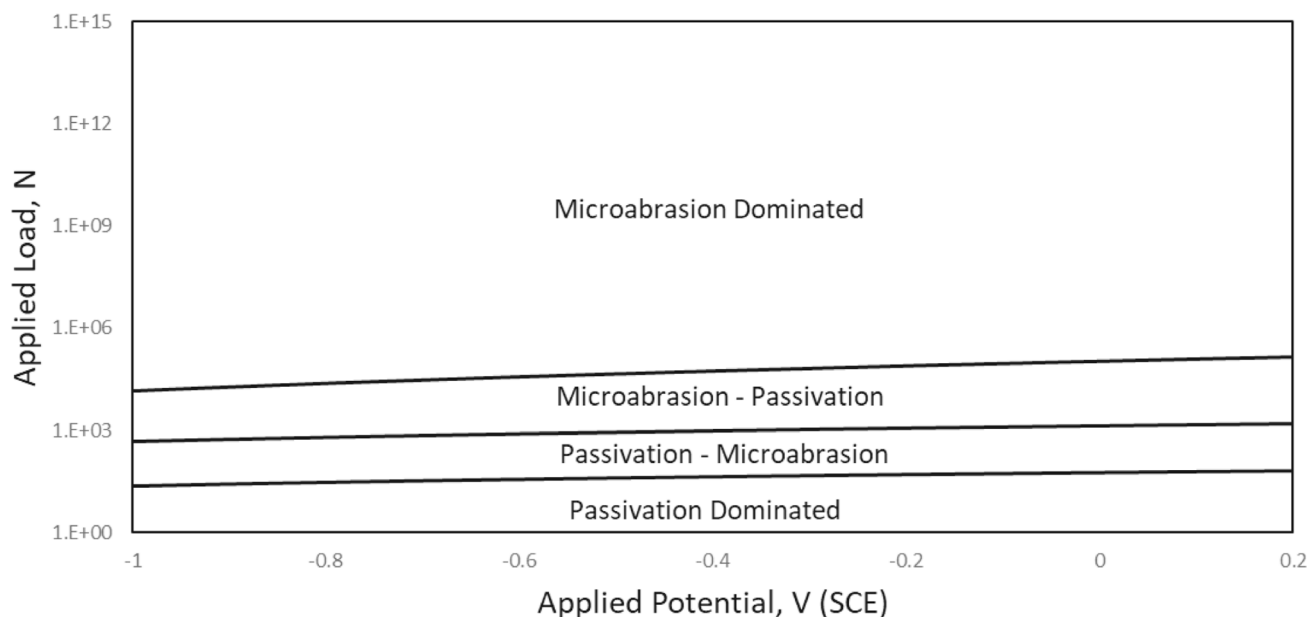
3.1 Effect of Increasing the pH on Applied Load: Applied Potential Maps for 100 μm Abrasive Particles

The two metals studied here, namely mild steel (Fe) and titanium (Ti), do not only have different mechanical

properties but they also show very different thermodynamic responses to corrosion mediums, as evident from their Pourbaix diagrams (in Figs. 1, 2). Both Fe and Ti show a transition from dissolution (or active corrosion) to passivation as the potential and pH were varied. However, the stability regimes of dissolution and passivation for Ti are significantly different than those of Fe. In particular, the dissolution and passivation regimes of Ti commence



(a)



(b)

Fig. 4 Applied load—applied potential regime maps for **a** Fe and **b** Ti under solution pH 7 and particle size of 100 μm

at significantly lower potentials compared to Fe. Consequently, the microabrasion-corrosion maps constructed in this study (Figs. 3, 4, 5, 6, 7, 8, 9) showed significantly different material degradation regimes for the Fe and Ti in the modelling conditions studied.

The microabrasion- corrosion regime and wastage maps, Fig. 3, 4, 5, 6 and 7, are given as applied load vs applied

potential map constructed for the abrasant size of 100 μm at various pH. In Fig. 3, at pH 3, the Fe showed only dissolution-dominated regimes, whereas the Ti showed both dissolution and passivation-dominated regimes in the corrosion potential range (from -1 to 0.2 V SCE) modelled. This was consistent with the trends from the Pourbaix diagram (Figs. 1, 2). It should be noted that the corrosion

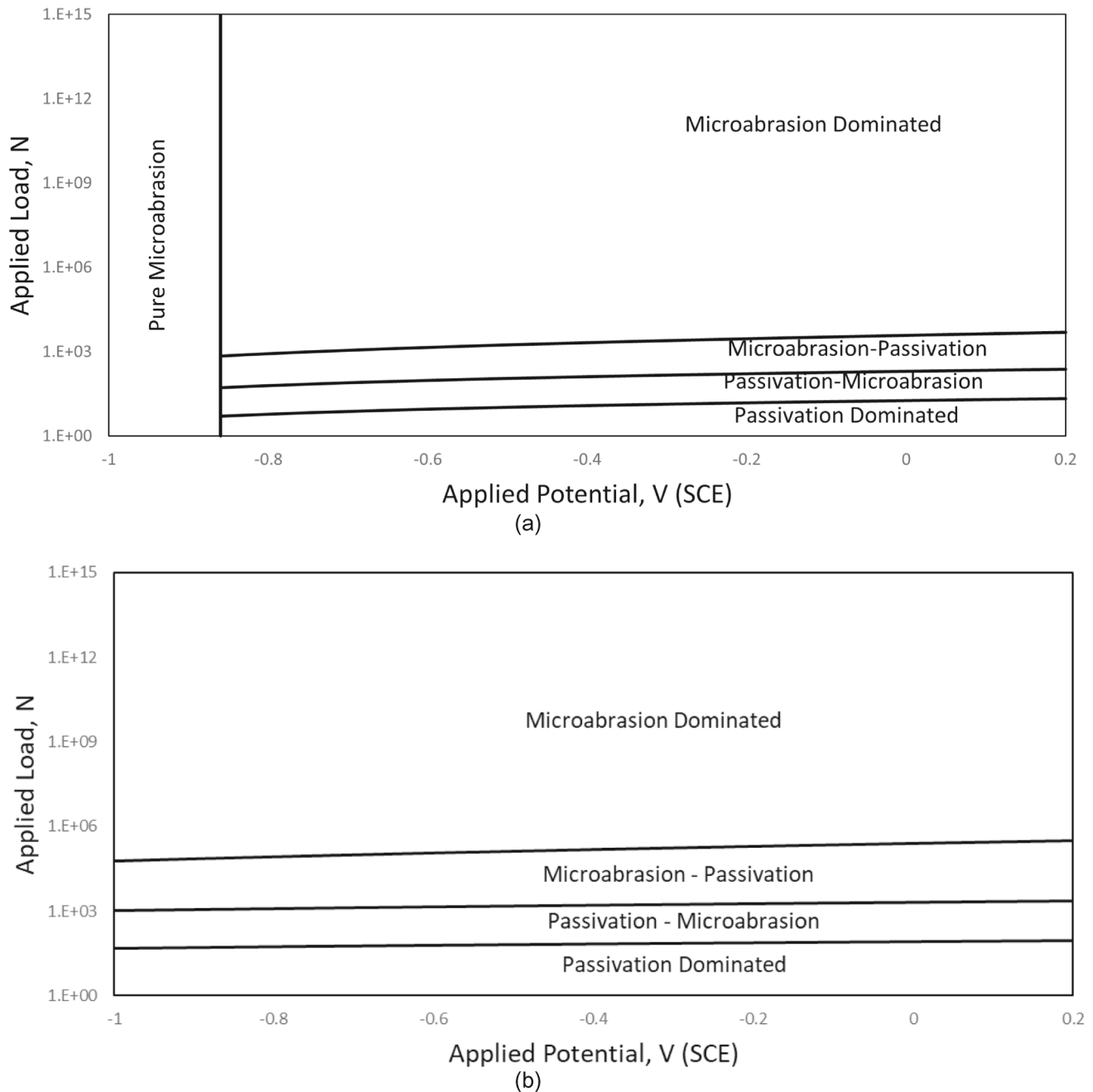


Fig. 5 Applied load—applied potential regime maps for **a** Fe and **b** Ti under solution pH 9 and particle size of 100 μm

potential values in all the maps reported here are given with respect to saturated calomel electrode (SCE), consistent with the earlier erosion-corrosion mapping work [13, 17]. Additional interesting features in Fig. 3 include the following. The region of "pure microabrasion" was shown only by the Fe (Fig. 3a) rather than the Ti (Fig. 3b); this is due to the Fe being immune to corrosion at lower potentials (up to -0.86 V SCE), resulting in the only wear mechanism dominated in these conditions was microabrasion. Additionally, in the active corrosion potential range, the

dissolution-dominated behaviour of the Ti extends to a significantly higher load compared with the Fe; this may be due to Ti having a much larger exchange current density than Fe leading to the rate of corrosion being much larger for the Ti.

When solution pH was increased to 7 (Fig. 4), the passive potentials for both the Fe and Ti shifted to lower values. Consequently, at pH 7, the Fe showed both dissolution and passivation-dominated regimes, whereas the Ti showed only passivation-dominated regimes in the condition modelled. These behaviours are again consistent with the Pourbaix

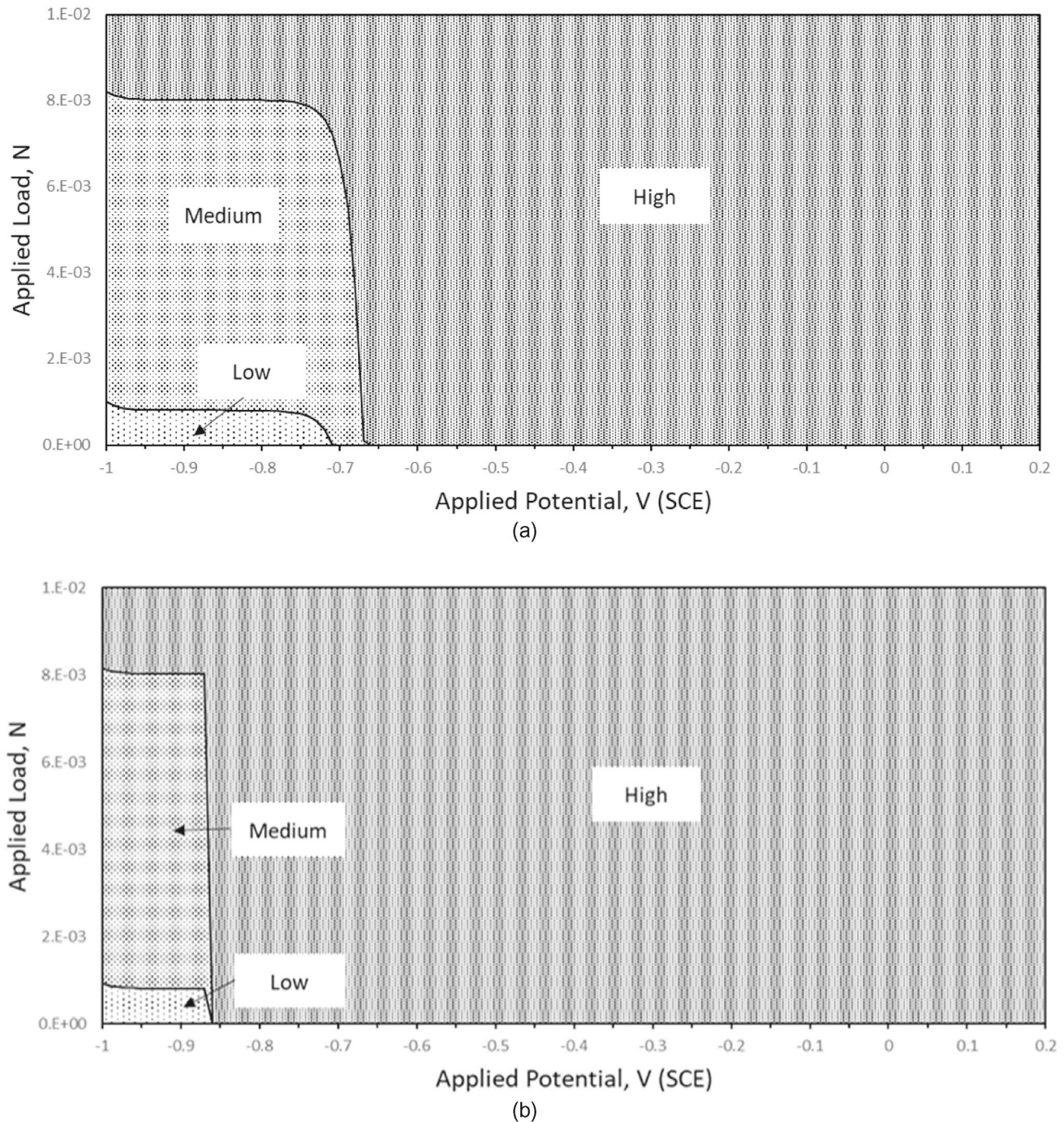


Fig. 6 Applied load—applied potential wastage maps for Fe under **a** pH 3 and 7, **b** pH 9 (particle size of 100 μm)

diagram of the metals (Fig. 1, 2). Further comparing Fig. 3 with Fig. 4 revealed the following. In the active corrosion potentials, increases in solution pH from 3 to 7 had no effect on the transition load to the dissolution-dominated regimes of the Fe. However, in the passive potential range, increase in pH significantly affected the passivation-dominated regimes of both the Fe and Ti. The Ti showed higher transition load to the passivation-dominated region when

solution pH increased from 3 to 7, whereas the Fe showed passivation-dominated regions at pH 7, but not at pH3.

As the solution pH was further increased to 9 (Fig. 5), the passive potential for both the Fe and Ti further lowered. As a result, the regime maps for both the Fe and Ti are dominated by the passivation process. Additionally, comparing Fig. 3 with Fig. 4 revealed that the transition load to passivation-dominated region for both Fe and Ti was increased with the

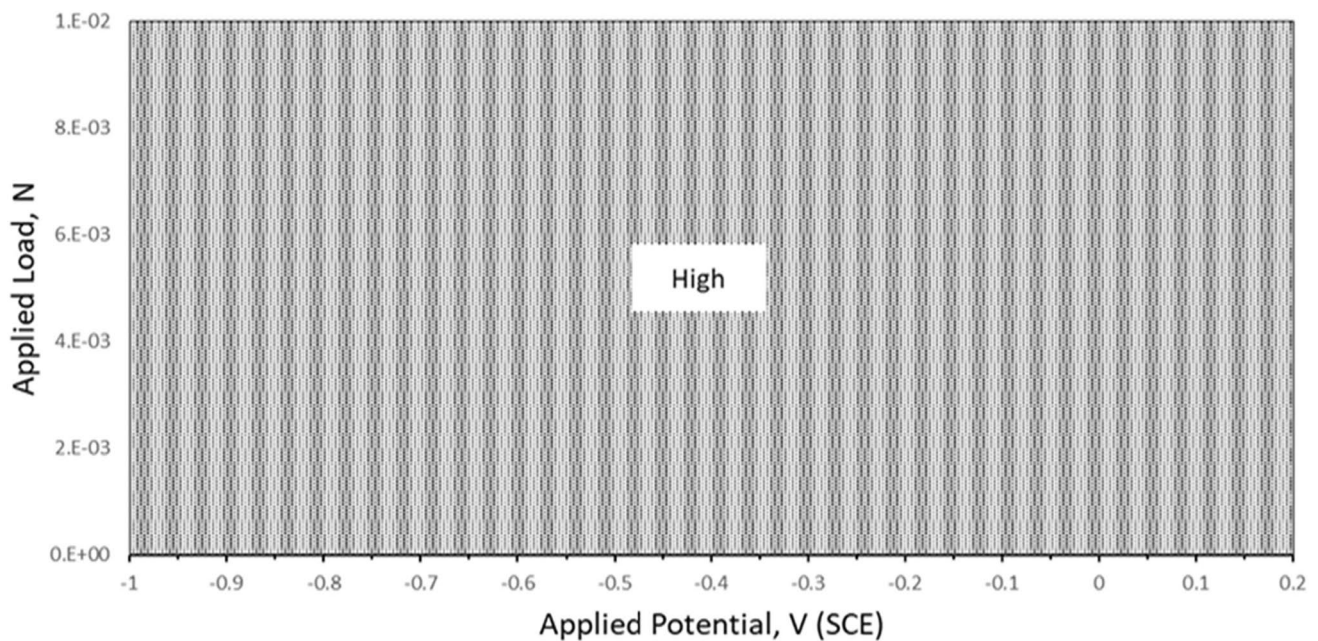


Fig. 7 Applied load—applied potential wastage maps for Ti under pH 3, 7 and 9 (particle size of 100 μm)

increase in solution pH. This may be due to the thickness of the passive film being increased at a higher pH. According to the assumptions used in this work, the mechanism of material removal in the passivation region is supported only by the removal of the passive film from the target surface; therefore, the higher the passive film thickness, the higher the transition load required for the passivation-dominated regions.

The microabrasion-corrosion wastage maps of the Fe and Ti, Figs. 6 and 7, are given as applied load vs applied potential area maps for the abradant particle size of 100 μm at various solution pHs. The wastage regimes of the Fe, Fig. 6, were dependent on the applied potential; the low and medium wastage regions of the Fe were associated with the lower potentials, where the microabrasion-corrosion process was affected by the immunity and dissolution behaviour of the metal consistent with the Pourbaix diagram (Fig. 1).

The wastage map for Fe was identical at the solution pH of 3 and 7; this is because the rate of wastage was independent of the applied load in the immunity region (i.e. up to -0.86 V SCE), after which the wastage rate increased very fast in the dissolution affecting conditions shown by rapid tapering of the regime boundaries for both pH 3 and pH 7. However, when solution pH was increased to 9, the Fe did not undergo the dissolution process rather showed the transition from immunity to passivation. As a result, the tapering which was seen for pH 3 and pH 7 was not seen here; instead, there was a rapid change from low and medium metal wastage rates to a high wastage rate in the passivation conditions.

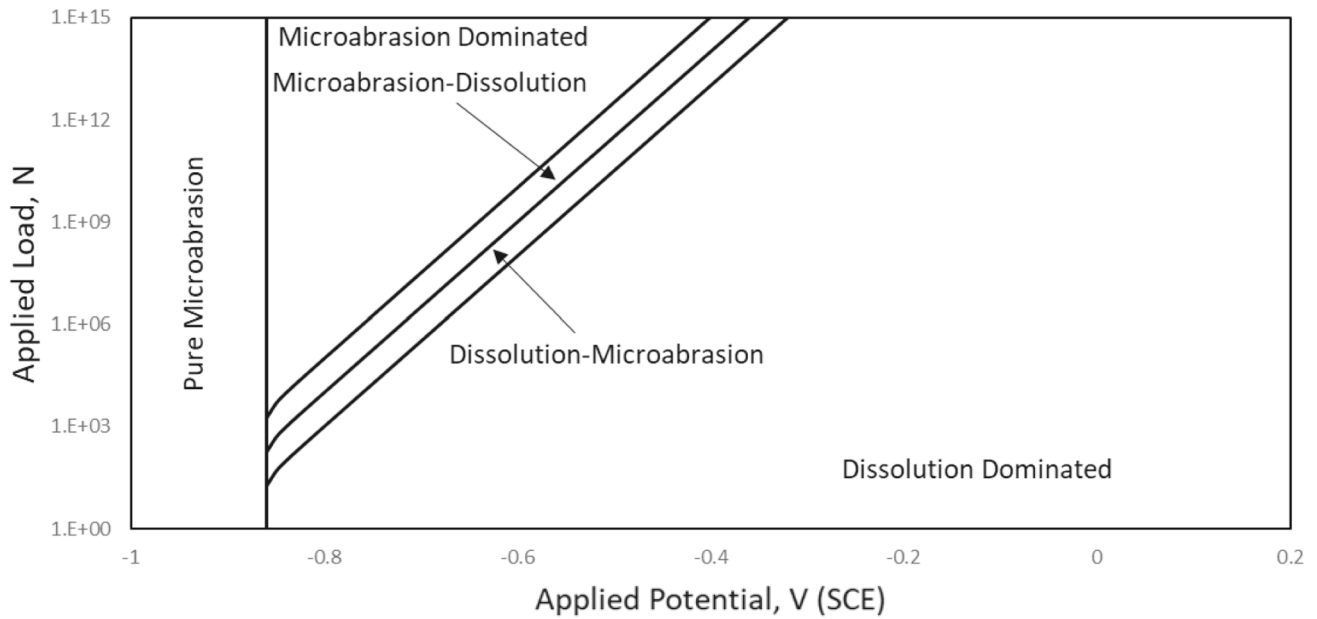
The wastage maps of the Ti, Fig. 7, showed only the high wastage area for the solution pH of 3, 7 and 9 attempted in this study. This is mainly because the microabrasion-corrosion rate of the Ti under the influence of both dissolution and passivation was high. Comparing the wastage maps of the Fe and Ti, Fig. 6 and 7, further revealed the following. When the corrosion regime is passivation, both the Fe and Ti showed high wastage; however, when the corrosion regime was dissolution dominated, the wastage rate of Fe was significantly lower than the Ti; this is due to the Ti having a much greater exchange current density than the Fe leading to the corrosion rate contributing to the overall microabrasion-corrosion wastage rate of the metal.

3.2 Effect of Changing the Abrasive Particle Size on Applied Load: Applied Potential Maps

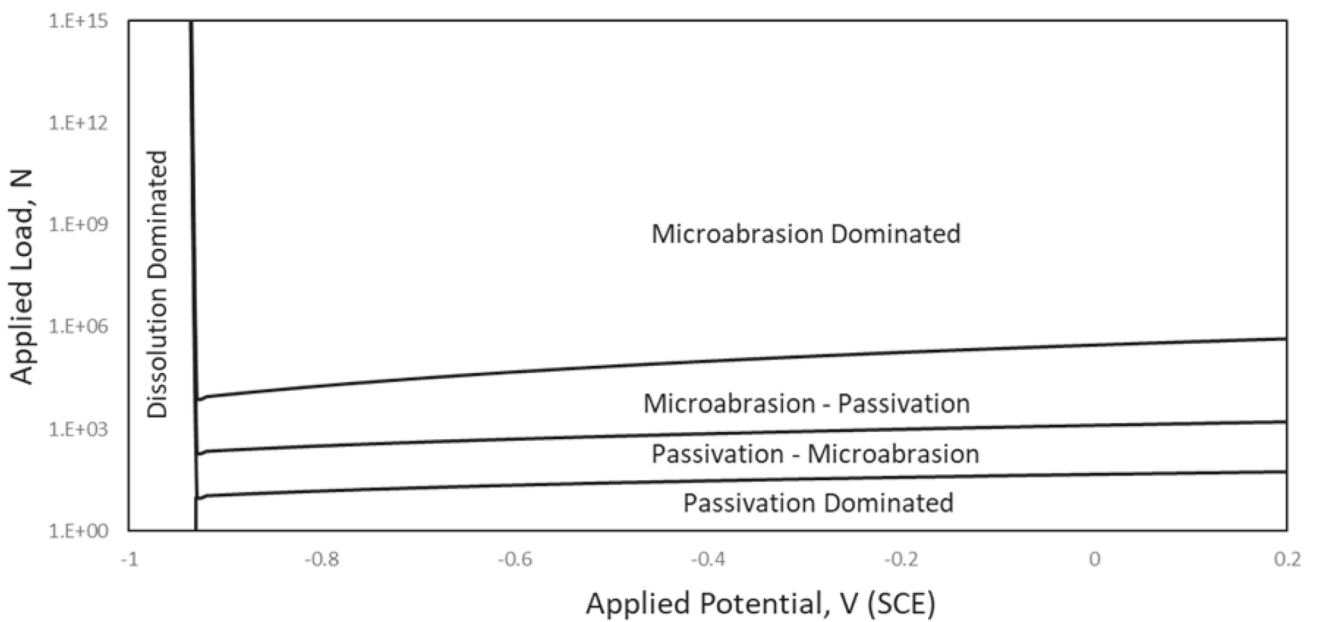
Effect of particle size on the regime and wastage maps of the Fe and Ti were assessed for pH 3. Comparing the maps for the abradant particle size of 50 μm , Fig. 8 and 9, with those for the abradant size of 100 μm , Fig. 3, 6a and 7, revealed the following.

The regime map for the Fe, Figs. 3a and 8a, showed the transition load to the regime boundaries increased when particle size was increased. The wastage maps for Fe, Figs. 6a and 9a, similarly show the transition load to the wastage boundaries increased with the particle size.

The Ti, Fig. 3b and 8b, also showed higher transition load to regime boundaries when the abrasive particle size was increased. However, the wastage map of the Ti, Figs. 6b



(a)



(b)

Fig. 8 Applied potential—applied load regime maps for **a** Fe and **b** Ti under solution pH 3 and particle size of 50 μm

and 9b, showed only the high wastage region for both the abrasive particle size studied. This is mainly because of the high exchange current density of the metal, leading to a high dissolution rate in the modelling conditions used.

4 Discussion

4.1 Microabrasion-Corrosion Regime and Wastage Maps for Pure Metals

The microabrasion-corrosion regime maps (Figs. 3, 4, 5) help to identify the underlying dominating mechanisms of

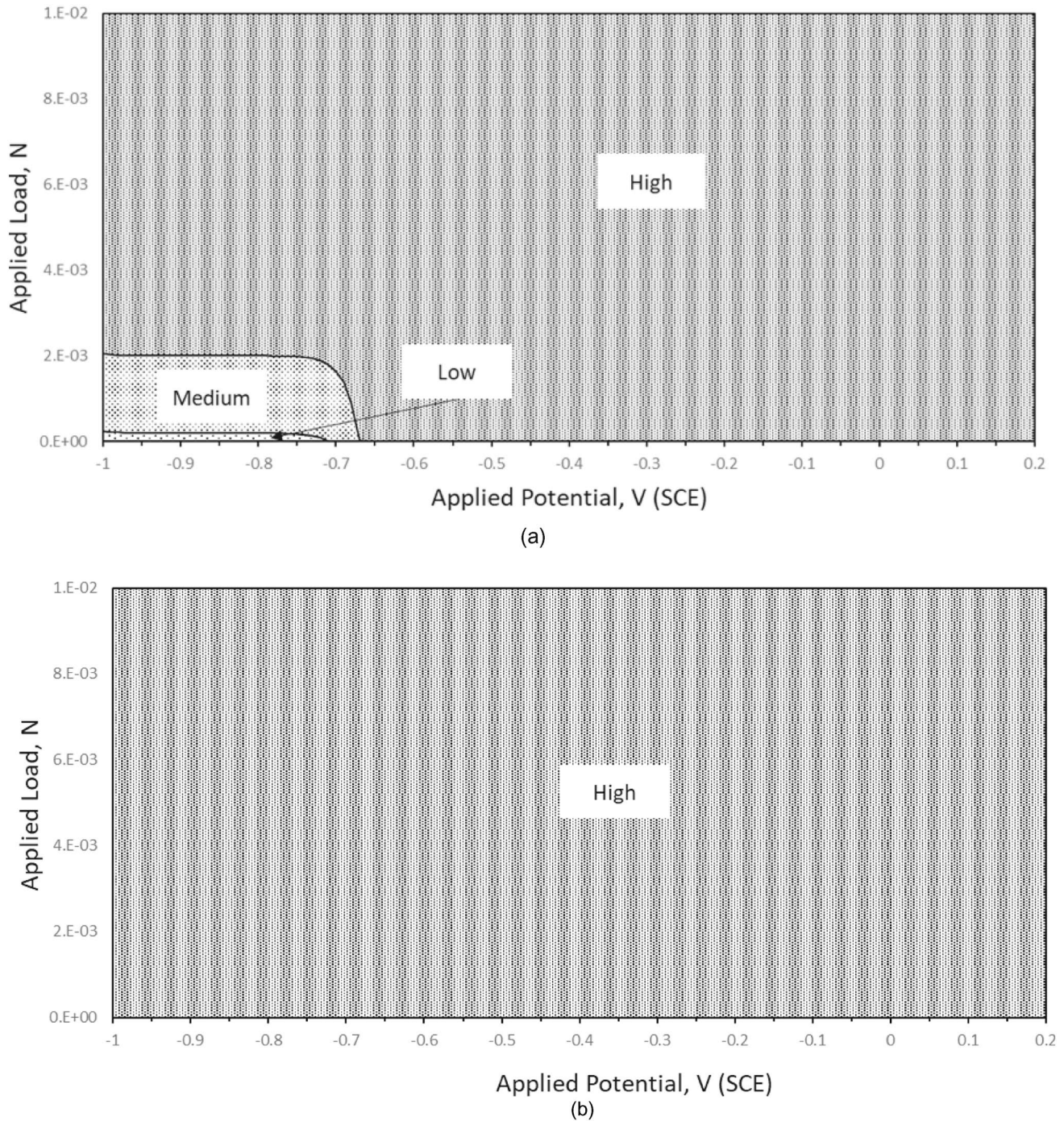


Fig. 9 Applied potential—applied load wastage maps for **a** Fe and **b** Ti under solution pH 3 and particle size of 50 μm

degradation as a function of operating parameters, which were chosen for this study as the applied load and corrosion potential. Identification of dominating mechanisms provides a valuable logical understanding towards formulating a degradation mitigation methodology. For example, if the dominating mechanism is “dissolution” only, then a degradation mitigation methodology should focus on corrosion

mitigation methodology only (not microabrasion); hence reducing the overall maintained cost.

The regime maps of the two pure metals, Fe and Ti, show a significant difference in the microabrasion-corrosion regime in the modelling conditions studied; however, the general trend is dependent on the corrosion only behaviour observed in the Pourbaix diagrams (Fig. 1, 2).

Albeit both the Fe and Ti show active–passive transitions towards lower pH values, the corrosion potential required for the active–passive transition is significantly lower for the Ti compared with the Fe. Consequently, in this study, the regime maps for Ti show active–passive transition only at pH 3, whereas that for the Fe extends up to pH 7. Additionally, due to the Ti having a higher exchange current density compared with the Fe, the rate of dissolution of the Ti is significantly higher than the Fe; as a result, the ratio of the pure corrosion to the microabrasion rates (K_c/K_a) in the active corrosion potentials is significantly higher for the Ti. Therefore, the dissolution-dominated regimes for the Ti extend to a significantly higher transition load compared with the Fe, as shown in Fig. 3.

In the passivation region, the transition load to regime boundaries is significantly higher for the Ti compared with the Fe. This is because the passive film thickness formed on the Ti surface is significantly higher than the Fe, according to Eq. 19. As a result, more passive film is removed from the Ti during the microabrasion-corrosion process at the passive potentials.

The wastage maps (Figs. 6, 7) show the variation of wastage bands as a function of process parameters, which were considered as the applied load and corrosion potentials in this study. The wastage bands are considered as Low, Medium and High, and are based on subjective limits that depend on the anticipated lifetime of the material in the exposure conditions. Wastage maps can potentially be a valuable tool for estimating the lifetime of a component and provide a basis for optimising the process by changing operating parameters. Furthermore, if such wastage maps are developed for a range of materials, material selection can be facilitated by comparing the low wastage performance of each metal in the operating conditions to be used.

In the modelling conditions used, the wastage maps of Ti for the pH 3, 7 and 9 show only the high wastage region, whereas that of the Fe shows the low, medium and high wastage regions. This suggests that the Ti offers significantly lower microabrasion-corrosion resistance compared with the Fe in the process conditions modelled. To understand the exact reason for the difference in the wastage behaviour of the Ti and Fe will require experimental results on the microabrasion-corrosion interactions of the materials covering both synergistic and additive effects. However, a reason may be that the Ti has significantly higher exchange current density compared with the Fe; as a result, both the pure corrosion rate in the active corrosion conditions and the additive effect of the microabrasion-corrosion in the passive conditions are significantly higher for the Ti compared with the Fe.

Regarding the effect of abrasive particle size on the microabrasion-corrosion maps, the results show (Fig. 3, 6a, 7, 8, 9) the rate of microabrasion-corrosion increases with the decrease in abrasive size. This is consistent with the expectation that (in a ball-cratering microabrasion test) the rate of wear increases with the decrease in abrasive particle size mainly due to higher particle concentrations in ball-substrate contact area when the particle size is smaller. Consequently, the wastage map for the Fe, Fig. 6a and 9a, showed a larger extent of the high wastage area when the abrasive particle size was reduced.

The microabrasion-corrosion maps produced in this study are greatly dependent on the accuracy of the microabrasion and corrosion models and the limitations of the current work discussed further below.

4.2 Model Limitations

The microabrasion-corrosion maps developed in this work can potentially be used as tools for material selection for microabrasion-corrosion applications, such as prosthesis material selection for human joints. However, there are limitations to the microabrasion-corrosion maps presented here.

This modelling work used predictive mathematical equations from the literature and constructed the models based on the wear behaviour observed in a micro-scale abrasion test (also known as the ball-cratering abrasive wear tests) [1–3, 5, 6]. The predictive microabrasion rate equation was considered as a published equation similar to the Archard equation, which relied on an empirical constant [15]. The current modelling study used the published values of the empirical contact for Ti and Fe, and did not verify those through appropriate laboratory experiments. In addition, there is the unavailability of a suitable mechanism-based microabrasion-corrosion predictive model in the literature, and a derivation of such models may improve the accuracy of the maps further.

In this work, the microabrasion-corrosion process was additive in the passivation conditions; this is a simplistic assumption. This may not be reflective of the true interactions between these two processes, which can be synergistic, additive, subtractive or antagonistic [1, 14, 26]. The true synergistic effect is observed in metallic composite-based coatings, but in monolithic metals, the additive effect can be applied when the passive film adheres strongly to the metal surface and can protect the metal from further corrosion. Therefore, consideration of the additive effect is a reasonable assumption in this study. Still, clearly, all the different types of microabrasion-corrosion interactions need to be incorporated in future studies.

The model also assumed that there was only one type of microabrasion taking place. This model assumed that only two-body abrasion took place regardless of the system conditions, which was simplistic. It can be seen from the literature that the type of microabrasion which would be observed would be dependent on system conditions, and this would affect the rate of microabrasion [1, 3, 14]. This needs to be considered in future studies.

5 Conclusions

1. Mathematical models for microabrasion-corrosion degradation have been developed and finally used to construct microabrasion-corrosion maps for mild steel and pure titanium.
2. The microabrasion-corrosion maps have been constructed in the form of regime and wastage maps; the regime maps identify the underlying material mechanisms, whereas the wastage maps identify the wastage rate in the form of low, medium and high wastage bands.
3. The effect of abrasive particle size and solution pH have also been shown on the maps.
4. Ti offers significantly lower microabrasion-corrosion resistance compared with Fe in the conditions modelled where there was a tribological interaction with corrosion. Although Ti is generally regarded as a corrosion resistant metal in passive conditions, in this microabrasion modelling, its performance is dependent on the tribological conditions. Where the impact can remove the oxide, regrowth may occur resulting in high microabrasion-corrosion rates.

Author Contributions F.W.R. contributed towards data curation and writing- original draft preparation. B.D.J. contributed towards conceptualization, supervision, research methodology, and writing—review and editing. I.Z. contributed towards supervision and visualization. M.M.S. contributed towards conceptualization, supervision, research methodology, and writing—review and editing.

Funding The authors declare that no funds, grants or other support were received during the preparation of this manuscript.

Availability of Data and Materials The datasets generated during and/or analysed during the current study are available from the corresponding author on reasonable request.

Declarations

Competing interest The authors have no relevant financial or non-financial interests to disclose.

Ethical Approval Not applicable.

Open Access This article is licensed under a Creative Commons Attribution 4.0 International License, which permits use, sharing, adaptation, distribution and reproduction in any medium or format, as long as you give appropriate credit to the original author(s) and the source, provide a link to the Creative Commons licence, and indicate if changes were made. The images or other third party material in this article are included in the article's Creative Commons licence, unless indicated otherwise in a credit line to the material. If material is not included in the article's Creative Commons licence and your intended use is not permitted by statutory regulation or exceeds the permitted use, you will need to obtain permission directly from the copyright holder. To view a copy of this licence, visit <http://creativecommons.org/licenses/by/4.0/>.

References

1. Stack MM, Jawan H, Mathew MT (2005) On the construction of micro-abrasion maps for a steel/polymer couple in corrosive environments. *Tribol Int* 38:848–856
2. Adachi K, Hutchings IM (2003) Wear-mode mapping for the micro-scale abrasion test. *Wear* 255(1–6):23–29
3. Rutherford K, Hutchings I (1997) Theory and application of a micro-scale abrasive wear test. *J Test Eval* 25(2):250–260
4. Sadiq K, Black RA, Stack MM (2014) Bio-tribocorrosion mechanisms in orthopaedic devices: Mapping the micro-abrasion-corrosion behaviour of a simulated CoCrMo hip replacement in calf serum solution. *Wear* 316:58–69
5. Stack M, Mathew M (2003) Micro-abrasion transitions of metallic materials. *Wear* 255(1):14–22
6. Hayes A, Sharifi S, Stack M (2015) Micro-abrasion-corrosion maps of 316L stainless steel in artificial saliva. *J Bio- Tribo-Corros* 1(2):1–15
7. SrinivasaPai P, Mathew MT, Stack MM, Rocha LA (2008) Some thoughts on neural network modelling of microabrasion–corrosion processes. *Tribol Int* 41(7):672–681
8. Archard JF (1953) Contact and rubbing of flat surfaces. *J Appl Phys* 24(8):981–988
9. Nothnagel G (1993) Wear resistance determination of coatings from cross-section. *Surf Coat Technol* 57:151–154
10. Rutherford KL, Hutchings IM (1996) A micro-abrasive wear test, with particulate applications to coated systems. *Surf Coat Technol* 79:231–239
11. Kusano Y, Van Acker K (2004) Methods of data analysis for the micro-scale abrasion test in coated substrates. *Surf Coat Technol* 183:312–327
12. Rutherford KL, Trezona RI, Ramamurthy AC, Hutchings IM (1997) The abrasive and erosive wear of polymeric paint films. *Wear* 203–204:325–334
13. Stack MM, Jana BD (2004) Modelling particulate erosion–corrosion in aqueous slurries: some views on the construction of erosion-corrosion maps for a range of pure metals. *Wear* 256(9):986–1004
14. Stack M, Rodling J, Mathew M, Jawan H, Huang W, Park G, Hodge C (2010) Micro-abrasion–corrosion of a Co–Cr/UHMWPE couple in Ringer's solution: an approach to construction of mechanism and synergism maps for application to bio-implants. *Wear* 269(5–6):376–382
15. Rabinowicz E, Dunn L, Russell P (1961) A study of abrasive wear under three-body conditions. *Wear* 4(5):345–355
16. Popov VL (2017) Contact mechanics and friction: physical principles and applications. Springer, Berlin
17. Stack MM, Corlett N, Zhou S (1997) A methodology for the construction of the erosion-corrosion map in aqueous environments. *Wear* 230:474–488

18. Pourbaix M (1974) Atlas of electrochemical equilibria in aqueous solutions. National Association of Corrosion Engineers, Houston
19. Sundararajan G, Shewmon P (1983) A new model for the erosion of metals at normal incidence. *Wear* 84(2):237–258
20. National Library of Medicine (2021) PubChem compound summary for CID 26042, titanium dioxide. <https://pubchem.ncbi.nlm.nih.gov/compound/Titanium-dioxide>. Accessed 25 Aug 2021
21. Wendt H, Spinace EV, Oliveria Neto A, Linardi M (2005) Electrocatalysis and electrocatalysts for low temperature fuel cells: fundamentals, state of the art, research and development. *Quim Nova* 28(6):1066–1075
22. Wen-Wei Hsu R, Yang C-C, Huang C-A, Chen Y-S (2004) Electrochemical corrosion properties of Ti–6Al–4V implant alloy in the biological environment. *Mater Sci Eng A* 380:100–109
23. Royal Society of Chemistry (2021) Titanium. <https://www.rsc.org/periodic-table/element/22/titanium>. Accessed 31 Mar 2021
24. Luo Y, Yang L, Tian M (2013) 3—Application of biomedical-grade titanium alloys in trabecular bone and artificial joints. *Biomater Med Tribol* 1:181–216
25. Saravanan K, Sumit B, Nithilaksh PL, Narayanan PR (2015) Evaluation of elastic properties of CP Ti by three different techniques. *Mater Sci Forum* 830–831:195–198
26. Stack M, Mathew M, Hodge C (2011) Micro-abrasion–corrosion interactions of Ni–Cr/WC based coatings: approaches to construction of tribo-corrosion maps for the abrasion–corrosion synergism. *Electrochim Acta* 56(24):8249–8259

Publisher's Note Springer Nature remains neutral with regard to jurisdictional claims in published maps and institutional affiliations.